Journal of Sound and Vibration (1996) **190**(1), 21–40

FREE AND FORCED VIBRATION OF A CYLINDRICAL SHELL WITH A FLOOR PARTITION

J. Missaoui, L. Cheng and M. J. Richard

Department of Mechanical Engineering, Laval University, Québec, Canada, G1K 7P4

(*Received* 16 *September* 1994, *and in final form* 10 *April* 1995)

A general formulation is presented to study the modal characteristics and the vibrational response of a cylindrical shell with a floor partition. The model is based on a variational formulation in which the structural coupling is simulated using artificial spring systems. In order to show the accuracy of the approach, numerical results are carried out with special attention paid to the characterization of the shell–floor connection. Natural frequencies and mode shapes are determined. Results are compared with previous publications and also with the finite element method. The effects of individual artificial springs and the in-plane motion of the floor on the modal characteristics are discussed. Finally, the forced response analysis is performed to illustrate the physical phenomena due to the shell–floor coupling. The obtained results show the efficiency of the method in handling a wide spectrum of structural coupling.

1. INTRODUCTION

Cylindrical shell structures have been widely investigated by researchers as a basic model to simulate aircraft structures. From the very early work to the recently published papers on the issue, one attains a good understanding of the fundamental phenomena of the cylindrical structures in terms of the dynamic behavior or the noise transmission characteristics [1–6]. Compared to the cylindrical shell, the partitioned shell with a longitudinal floor seems to be a more realistic model. Due to the mechanical coupling between the floor and the shell, the dynamic behavior of the combined structure becomes relatively complicated. Consequently, much less information is available in the literature. From the sound proofing point of view, the full understanding of the coupling behavior of the system is crucial for further cabin noise analysis. Hence, flexible dynamic models which can be extended for vibro-acoustic analysis should be developed.

Several papers are available for studying the free vibration of a partitioned shell. The first analytical model developed was reported by Peterson and Boyd [7], who used the Rayleigh–Ritz technique to study the free vibration of a cylindrical shell with an internal floor. In that paper, the effects of several parameters such as rigid or hinged joint, thickness of the structure and the position of the floor on the frequencies and the mode shapes were analyzed. More recently, Langley [8] studied the free vibration of a simply supported stiffened cylindrical structure by using a dynamic stiffness technique. In his study, three structural elements were used to model a cylindrical shell with an internal floor. Irie *et al*. [9] studied the free vibration of non-circular cylindrical shells with longitudinal partitions. Using the transfer matrix, their method could be applied to shells with any circumferential profiles with simply supported boundaries. In addition to analytical approaches, the finite

0022–460X/96/060021 + 20 $12.00/0

element method (FEM) has also been used to study this kind of problem. Unruh and Dobosz [10] presented a structure model using the finite elment method to extract structural modes at low frequencies. Despite the fact that the FEM usually needs large and fast computational facilities, it offers a powerful method with which to treat complex structures. In the category of plate–shell structure, Huang and Soedel [11] studied the structural response of circular plates combined to a cylindrical shell at any axial position by using the receptance method. The receptance formulation has been proved to be efficient and simple to use under several circumstances, specially for the case of point coupling or line coupling with symmetric geometry for which a spatial distribution assumption of the force can, *a priori*, be made. However, the receptance method becomes difficult to exploit for a shell partitioned by a longitudinal floor, since no information on the force distribution along the joint is *a priori* available.

Apart from those investigations specifically related to plate–shell combined structures, considerable efforts have been made to develop more physical approaches with wider fields of applications. It is evident that for such combined structures, there is no other alternative than to develop approximate solutions. The actual trend is to use a physical base as much as possible before a numerical approach is engaged. In this line of thought, let us mention the newly developed artificial spring approach, with regard to which the present paper introduces further developments. Spring systems were first used in the literature to study the support conditions of a single structure by authors such as Gorman [12], Warburton and Edney [13] and Mizusawa [14]. Then, one found the utilization of the spring set-up for more complicated structures such as the coaxial double shell. Yamada *et al*. [15] used springs to study the free vibration of two coaxial circular cylindrical shells; the semi-analytical approach was based on the transfer matrix. In his work, the springs are included in the mathematical model by the equilibrium equations at the interconnected regions. Recently, the spring set-up was used in a different way to characterize a mechanically coupled structure [16–18]. By allowing a wide variation range of spring stiffness, different joint conditions can be simulated with the artificial spring technique. Yuan and Dickinson [16,17] investigated free vibrations of straight and curved beam components and varieties of coupled plates. Cheng and Nicolas [18] studied a coupled system comprising a cylindrical shell closed at one end by a circular plate. By including the potential energy of the spring and using Hamilton's principle, it was pointed out that the established framework opened a door to further forced vibration analysis and eventually vibro-acoustic analysis [19]. However, up to now, the technique has only been used for simple structures. Even for the work reported in reference [18], which is the most complicted case treated with the method, only flexural coupling is considered.

The present work can be considered as a development of the artificial spring technique for a more complicated structure. For the case of a cylindrical shell coupled to an internal floor, the objective is to investigate the following issues:

(1) To develop a formulation on the free and forced vibrations of a floor-partitioned shell, which can be eventually extended to include internal acoustic effects. The approach is therefore extended to treat a complex structure in which the mechanical coupling is a three-dimensional one.

(2) To assess the feasibility and the efficiency of the approach with a closer look at the characterization of the coupling continuity at the junctions.

(3) To analyze different joint conditions ranging from free, through elastic to rigid connections and, among other parameters, to illustrate the sensitivity of the structure to the variation of the joint conditions.

It is hoped that the developed approach gives more physical insight than the purely numerical one and offers a greater flexibility for the design process. The paper first presents

the development of the analytical approach. Then numerical results are presented to show the accuracy, convergence and utility of the proposed formulation. Comparisons are made with existing results and the finite element method. Finally, the response of the structure with a radial point driving force is analyzed.

2. ANALYTICAL APPROACH

The classical Rayleigh–Ritz method is a powerful approach to the free vibration analysis of structures. It is well known that the trial functions should verify at least the geometrical boundary conditions (related to the translation and rotation) to ensure good results [21]. For combined structures, the so-called geometrical boundary conditions include the continuity of each sub-system at the junctions. This consideration makes the choice of the trial function very difficult. The use of an artificial spring system at a junction permits one to overcome this difficulty. As shown schematically in Figure 1, a virtual set of a distributed spring system is introduced at the structural junction for every permitted degree of freedom. Physically, by allowing the spring stiffness to become very high compared to the stiffness of the components, rigid connections are approximated. Moreover, by using an appropriate stiffness of the spring, an elastic junction can also be simulated. Mathematically, the use of artificial springs at the junctions replaces the geometric conditions (continuity of the motion) by corresponding dynamic conditions (strain energy of the springs). As a result, the choice of the trial functions is simplified, since the latter have only to verify the geometrical boundary conditions at the non-connected regions. Thus, the classical method can then be used by considering the spring system as a dynamic element.

2.1. EQUATIONS OF MOTION

The structure considered in the analysis consists of a thin finite circular cylindrical shell with a longitudinal floor partition. The co-ordinate system used is shown in Figure 2(a) (a list of symbols is given in Appendix B). The boundary conditions of the shell–floor structure are considered simply supported at the two ends ($x=0, x=L_s$); more specifically, for the shell, the boundary conditions are considered to be supported by a *shear diaphragm* [20] and the floor is simply supported. Considering an harmonic motion, the displacement functions of the shell in longitudinal (u_s), circumferential (v_s) and radial (w_s) directions are decomposed on the basis of the natural modes of the corresponding single shell:

$$\begin{Bmatrix} u_s \\ v_s \\ w_s \end{Bmatrix} = \sum_{\alpha=0}^{1} \sum_{m=1}^{\infty} \sum_{n_s=0}^{\infty} c_{mn_s}^{\alpha}(t) \begin{Bmatrix} a_{mn_s}\cos(n_s\theta - \alpha(\pi/2))\cos(m\pi x/L_s) \\ b_{mn_s}\sin(n_s\theta - \alpha(\pi/2))\sin(m\pi x/L_s) \\ 1\cos(n_s\theta - \alpha(\pi/2))\sin(m\pi x/L_s) \end{Bmatrix}, \tag{1}$$

where $\alpha=0$ (or 1) denotes symmetric (or antisymmetric) modes, and $(a_{mn_s}, b_{mn_s}, 1)$ is the normal eigenvector of the shell with a *shear diaphragm* condtion. The arbitrary constant

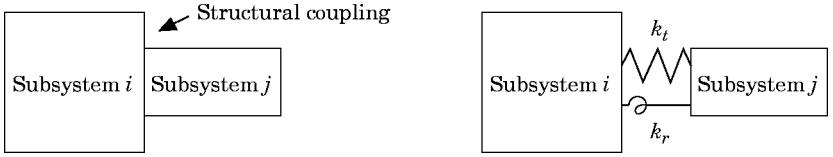

Figure 1. A schematic representation of the modelling of the coupling

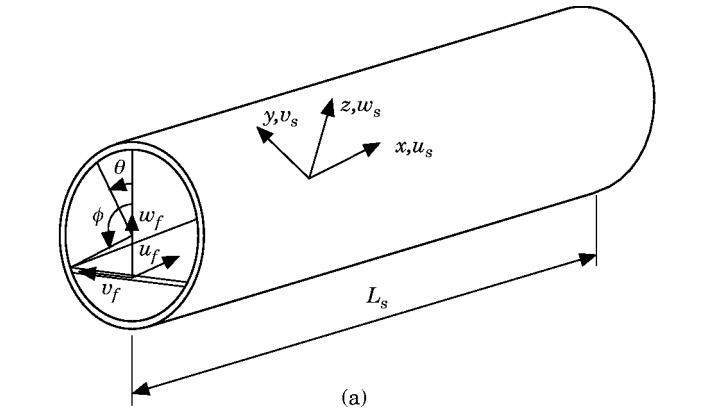

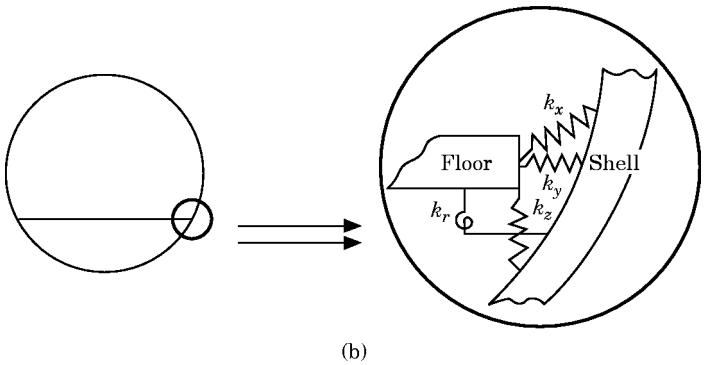

Figure 2. (a) A partitioned shell. (b) The artificial spring set-up.

$c^{\alpha}_{mn_s}$ is the coefficient to be determined by considering the shell–floor structure. For the floor, the displacement functions including the in-plane degree of freedom are expressed as

$$\begin{Bmatrix} u_f \\ v_f \\ w_f \end{Bmatrix} = \sum_{\alpha=0}^{1} \sum_{m=1}^{\infty} \sum_{n_f=0}^{\infty} \begin{Bmatrix} u^{\alpha}_{mn_f}(t)\cos((n_f\pi/b)y - \alpha(\pi/2))\cos(m\pi x/L_s) \\ v^{\alpha}_{mn_f}(t)\sin((n_f\pi/b)y - \alpha(\pi/2))\sin(m\pi x/L_s) \\ w^{\alpha}_{mn_f}(t)\cos((n_f\pi/b)y - \alpha(\pi/2))\sin(m\pi x/L_s) \end{Bmatrix}, \tag{2}$$

where u_f and v_f represent the in-plane displacements of the floor, and w_f is the transverse one (see Figure 2(a)). In the trial functions used above, trigonometric functions are chosen for the shell and the floor. The fact that we are using the natural modes of the uncoupled shell gives a more physical base for the shell portion, since the eventual coupling with the floor generates coupled modes which can be imagined to be a variant of the single shell. Moreover, as will be demonstrated later, the trigonometric functions used here separate not only symmetric and antisymmetric modes but also the terms with a different longitudinal half-wavenumber m. Consequently, the calculation for the search of the modes can be carried out for every single value of α and m. It should be pointed out that the two sets of trial functions verify the geometrical boundary conditions at the boundary excepting at the junction between the shell and the floor. In equation (1), only bending modes of the shell are used to reduce the size of matrices. The torsion and traction–compression modes can be easily added to the decomposition series [18].

However, it was demonstrated during our analyses that these supplementary terms have negligible influence on the results presented in the present paper, which are mainly at low and middle frequencies.

2.2. MODELING OF STRUCTURAL COUPLING

In order to insure structural coupling between the shell and the floor, artificial springs are inserted between the shell and the floor for every permitted degree of freedom. For each junction, three translational springs (k_x,k_y,k_z) are introduced along the x,y,z directions, and for the rotational coupling, a torsion spring is used (k_r). The spring set-up is schematically illustrated in Figure 2(b). Note that all springs stiffnesses are defined as uniformly distributed along the junctions. The joint conditions at the interconnected regions are characterized by means of the strain energy E_k stored in the artificial springs. This energy is a function of the stiffness and the relative motion (d_x,d_y,d_z,d_r) between the shell and the floor in each direction:

$$E_k=\frac{1}{2}\int_0^{L_s}\left[k_x\left(d_x^2\left(\frac{b}{2},\phi\right)+d_x^2\left(-\frac{b}{2},2\pi-\phi\right)\right)+k_y\left(d_y^2\left(\frac{b}{2},\phi\right)+d_y^2\left(-\frac{b}{2},2\pi-\phi\right)\right)\right.$$

$$\left.+k_z\left(d_z^2\left(\frac{b}{2},\phi\right)+d_z^2\left(-\frac{b}{2},2\pi-\phi\right)\right)+k_r\left(d_r^2\left(\frac{b}{2},\phi\right)+d_r^2\left(-\frac{b}{2},2\pi-\phi\right)\right)\right]\mathrm{d}x, \tag{3}$$

where

$$d_x=u_f-u_s, \qquad d_y=v_f-w_s\sin\phi-v_s\cos\phi,$$

$$d_z=w_f-w_s\cos\phi+v_s\sin\phi, \qquad d_r=\frac{\partial w_f}{\partial y}-\frac{1}{a}\left(\frac{\partial w_s}{\partial\phi}-v_s\right) \tag{4}$$

After using equations (1) and (2), one has

$$E_k=\sum_{\alpha}\sum_{m}(E_k)_m^{\alpha}, \tag{5}$$

with

$$(E_k)_m^{\alpha}=\sum_{n_s'}\sum_{n_s}R^1_{mn_sn_s'\alpha}c^{\alpha}_{mn_s'}c^{\alpha}_{mn_s}+\sum_{n_f'}\sum_{n_f}[R^2_{n_fn_f'\alpha}u^{\alpha}_{mn_f}u^{\alpha}_{mn_f'}+R^3_{n_fn_f'\alpha}v^{\alpha}_{mn_f}v^{\alpha}_{mn_f'}+R^4_{n_fn_f'\alpha}w^{\alpha}_{mn_f}w^{\alpha}_{mn_f'}]$$

$$+\sum_{n_s}\sum_{n_f}[R^{12}_{mn_sn_f\alpha}u^{\alpha}_{mn_f}+R^{13}_{mn_sn_f\alpha}v^{\alpha}_{mn_f}+R^{14}_{mn_sn_f\alpha}w^{\alpha}_{mn_f}]c^{\alpha}_{mn_s}. \tag{6}$$

In equation (6), n_s' and n_f' are the running indexes having the same meaning as n_s and n_f. All the terms involved in equation (6) are calculated as follows:

$$R^1_{mn_sn_s'\alpha}=S^x_{mn_sn_s'\alpha}+S^y_{mn_sn_s'\alpha}+S^z_{mn_sn_s'\alpha}+S^r_{mn_sn_s'\alpha}, \qquad R^2_{n_fn_f'\alpha}=k_xL_s\cos\frac{(n_f-\alpha)\pi}{2}\cos\frac{(n_f'-\alpha)\pi}{2},$$

$$R^3_{n_fn_f'\alpha}=k_yL_s\sin\frac{(n_f-\alpha)\pi}{2}\sin\frac{(n_f'-\alpha)\pi}{2},$$

$$R^4_{n_f n'_f \alpha} = L_s \left(\cos\frac{(n_f-\alpha)\pi}{2} \cos\frac{(n'_f-\alpha)\pi}{2} k_z + \frac{k_r n_f n'_f \pi^2}{b^2} \sin\frac{(n_f-\alpha)\pi}{2} \sin\frac{(n'_f-\alpha)\pi}{2} \right),$$

$$R^{12}_{mn_s n_f \alpha} = -k_x L_s a_{mn_s} \cos\frac{(n_f-\alpha)\pi}{2} \cos\left(n_s\phi - \alpha\frac{\pi}{2} \right),$$

$$R^{13}_{mn_s n_f \alpha} = -k_y L_s \sin\frac{(n_f-\alpha)\pi}{2} \left[\cos\left(n_s\phi - \alpha\frac{\pi}{2} \right) \sin\phi + b_{mn_s} \cos\phi \sin\left(n_s\phi - \alpha\frac{\pi}{2} \right) \right],$$

$$R^{14}_{mn_s n_f \alpha} = k_z L_s \cos\frac{(n_f-\alpha)\pi}{2} \left[b_{mn_s} \sin\phi \sin\left(n_s\phi - \alpha\frac{\pi}{2} \right) - \cos\phi \cos\left(n_s\phi - \alpha\frac{\pi}{2} \right) \right]$$

$$- \frac{k_r L_s}{ab} n_f \pi (n_s + b_{mn_s}) \sin\frac{(n_f-\alpha)\pi}{2} \sin\left(n_s\phi - \alpha\frac{\pi}{2} \right). \tag{7}$$

The calculations for $S^x_{mn_s n'_s \alpha}$, $S^y_{mn_s n'_s \alpha}$, $S^z_{mn_s n'_s \alpha}$ and $S^r_{mn_s n'_s \alpha}$ are given in Appendix A. It is worth observing from equation (5) that, for each pair of α and m, the potential energy can be evaluated and the total energy is simply the total sum. This observation leads to two conclusions. First, the symmetric and antisymmetric modes of the shell–floor structure are not coupled one from another, meaning that a symmetric shell mode can only be coupled with a symmetric mode of the floor, and the same is true for antisymmetric modes. Second, the modes with different half-wavenumber are totally independent. This point will be fully used during the manipulations for reducing the matrix size of the calculations.

2.3. COUPLING EQUATIONS

The whole system is characterized by using the classical Hamilton's principle, which needs the calculations of the kinetic and strain energy of the combined system, as well as the work done by the external driving forces. The resulting Hamiltonian is then substituted into Lagrange's equations to yield the governing equations. With q_i as generalized co-ordinate and L as the Lagrangian, one has

$$\frac{\mathrm{d}}{\mathrm{d}t}\left(\frac{\partial L}{\partial \dot{q}_i} \right) - \frac{\partial L}{\partial q_i} = F_i \qquad i = 1,2,3,4, \tag{8}$$

where F_i represents the generalized force. In our case q_i denotes each of the coefficients in the series described by equations (1) and (2) ($c^\alpha_{mn_s}, u^\alpha_{mn_f}, v^\alpha_{mn_f}, w^\alpha_{mn_f}$). By using the point driving forces acting at an arbitrary location of the cylindrical shell and applying Lagrange's equations to the system, one obtains the following coupling equations for the whole system:

$$M_{mn_s}(\omega^2_{mn_s} - \omega^2) c^\alpha_{mn_s} + \sum_{n'_s} (R^1_{mn_s n'_s \alpha} + R^1_{mn'_s n_s \alpha}) c^\alpha_{mn'_s} + \sum_{n'_f} R^{12}_{mn_s n'_f \alpha} u^\alpha_{mn'_f} + R^{13}_{mn_s n'_f \alpha} v^\alpha_{mn'_f} + R^{14}_{mn_s n'_f \alpha} w^\alpha_{mn'_f}] = F^\alpha_{mn_s},$$

$$\sum_{n'_f} \left[k^u_{mn_f n'_f \alpha} - \omega^2 \frac{h_f \rho L_s}{2} \beta_{n_f n'_f \alpha} \right] u^\alpha_{mn'_f} + \frac{K_f \pi^2 m}{4b} \sum_{n'_f} [(-2\nu n_f \beta_{n_f n'_f \alpha} + (\nu - 1) n'_f \gamma_{n_f n'_f \alpha})] v^\alpha{}_{mn'_f}$$

$$+\sum_{n_s'} R^{12}_{mn_s'n_f\alpha} c^{\alpha}_{mn_s'} = 0,$$

$$\sum_{n_f'} \left[k^{v}_{mn_fn_f'\alpha} - \omega^2 \frac{h_f \rho L_s}{2} \gamma_{n_fn_f'\alpha} \right] v^{\alpha}_{mn_f'} + \frac{K_f \pi^2 m}{4b} \sum_{n_f'} [(-2\nu n_f' \beta_{n_fn_f'\alpha} + (\nu - 1) n_f \gamma_{n_fn_f'\alpha})] u^{\alpha}_{mn_f'}$$

$$+\sum_{n_s'} R^{13}_{mn_s'n_f\alpha} c^{\alpha}_{mn_s'} = 0,$$

$$\sum_{n_f'} \left[k^{w}_{mn_fn_f'\alpha} - \omega^2 \frac{h_f \rho L_s}{2} \beta_{n_fn_f'\alpha} \right] w^{\alpha}_{mn_f'} + \sum_{n_s'} R^{14}_{mn_s'n_f\alpha} c^{\alpha}_{mn_s'} = 0. \tag{9}$$

where ω_{mn_s} is the *in vacuo* angular frequency of the shell with *shear diaphragm* conditions and M_{mn_s} is its generalized mass. $k^{u}_{mn_fn_f'\alpha}$, $k^{v}_{mn_fn_f'\alpha}$, $k^{w}_{mn_fn_f'\alpha}$ and K_f are given in Appendix A. The expressions for $\beta_{n_fn_f'\alpha}$ and $\gamma_{n_fn_f'\alpha}$ are also given in Appendix A. $F^{\alpha}_{mn_s}$ is given by

$$F^{\alpha}_{mn_s} = \sum_{i=1}^{N_f} \begin{Bmatrix} F^i_u \\ F^i_v \\ F^i_w \end{Bmatrix}^{\mathrm{T}} \begin{Bmatrix} [a_{mn_s} - (m\pi h_s/L_s)]\cos(n_s\theta_{si} - \alpha(\pi/2))\cos(m\pi x_{si}/L_s) \\ [b_{mn_s} + (n_s h_s/2a)]\sin(n_s\theta_{si} - \alpha(\pi/2))\sin(m\pi x_{si}/L_s) \\ \cos(n_s\theta_{si} - \alpha(\pi/2))\sin(m\pi x_{si}/L_s) \end{Bmatrix}. \tag{10}$$

In the above equation N_f harmonic forces with three components (F^i_u, F^i_v, F^i_w) along three axes are applied at arbitrary points (x_{si}, θ_{si}). By equating the forcing vector in equation (9) to zero, the eigenvalues and the eigenvectors can be computed and the mode shapes can then be reconstructed from equations (1) and (2). As for the forced vibration response, the average quadratic radial velocities of the shell, $\langle V_s^2 \rangle$, and the floor, $\langle V_f^2 \rangle$, are calculated by

$$\langle V_s^2 \rangle = \frac{\omega^2}{4} \sum_{\alpha=0}^{1} \sum_{m=1}^{\infty} \sum_{n_s=0}^{\infty} \epsilon_{n_s} c^{\alpha}_{mn_s} c^{*\alpha}_{mn_s}, \tag{11}$$

$$\langle V_f^2 \rangle = \frac{\omega^2}{bL_s} \sum_{\alpha=0}^{1} \sum_{m=1}^{\infty} \sum_{n_f=0}^{\infty} \sum_{n_f'=0}^{\infty} w^{\alpha}_{mn_f} w^{*\alpha}_{mn_f'}, \tag{12}$$

where $c^{*\alpha}_{mn_s}$ and $w^{*\alpha}_{mn_f'}$ are, respectively, the complex conjugates of $c^{\alpha}_{mn_s}$ and $w^{\alpha}_{mn_f'}$.

3. DISCUSSION OF THE COMPUTATIONAL RESULTS

In all calculations reported hereafter, the shell and the floor are assumed to have the same thickness and the same material properties. The data used are as follows: mass density $\rho = 7500\,\mathrm{kg/m^3}$; Poisson's ratio, $\nu = 0{\cdot}3$; Young modulus, $E = 2 \times 10^{11}\,\mathrm{N/m^2}$; radius, $a = 0{\cdot}254\,\mathrm{m}$; thickness, $h_f = h_s = 5{\cdot}08 \times 10^{-3}\,\mathrm{m}$, length, $L_s = 1{\cdot}27\,\mathrm{m}$. The floor position is specified with $\phi = 115^{\circ}$.

The limitation of the infinite series to a finite number of terms is a computational restriction. The general criterion for truncating the series is to assure the accuracy in the resulting solutions. In order to warrant this, the series is increased until no significant variations are considered. During the calculation, a careful convergence study has been carried out for both substructures (shell and floor separately) and the combined structure. As far as the floor is concerned, tests were made to verify the convergence and the accuracy

with a general boundary condition; the result shows a good agreement with the data available in the literature. As to the combined structure, the decomposition terms are increased until the resulting natural frequencies converge to stable values. Note that the calculations can be done for each pair of α and m, so that the truncation has only to be done for circumferential orders. In the present simulation ten circumferential terms for the shell and 20 terms for the floor including the in-plane motion ($n_s^* = 10$, $n_w^* = 10$, $n_u^* = n_v^* = 5$) are taken for the modal analysis. The truncation used for the forced response is specified in each case.

One of the most attracting features of the established model relies on its capability to simulate a wide range of variations of the coupling conditions, going from free to rigid attachments. It is therefore important to evaluate the lowest value to be attributed to the spring in order to insure a rigid attachment simulation. Moreover, such an analysis allows one to understand how the changes of the junction stiffness may affect the coupling of the combined structure. The variation of the frequency parameter Ω versus a normalized stiffness parameter $\bar{k}(\bar{k}_x, \bar{k}_y, \bar{k}_z, \bar{k}_r)$ for the first six *symmetric* modes is illustrated in Figure 3. The so-called frequency parameter is defined as $\Omega = a\omega[\rho(1-\nu^2)/E]^{1/2}$. The normalized stiffness parameters are defined with respect to the flexural rigidity of the floor ($\bar{k}_x = k_x a^3/D_f, \bar{k}_y = k_y a^3/D_f, \bar{k}_z = k_z a^3/D_f$ and $\bar{k}_r = k_r a/D_f$; $D_f = Eh_f^3/12(1-\nu^2)$). In this calculation, the stiffness parameters for all the springs are changed in a systematic way. The starting value is 10^{-4} and the final value is reached when no significant variation in the frequency parameter is observed. Also, the calculated mode shapes with several stiffness parameters are plotted in Figure 4. It can be seen from Figure 3 that when the stiffness parameter is increased, the frequency increases at different rates depending on the vibration mode. Generally speaking, one can notice the existence of three regions. Taking the sixth mode as an example, the three regions are denoted by A, B and C. In region A, we notice that the frequency is not significantly sensitive to the stiffness variation. With $\bar{k} = 10^{-4}$, Figure 4(a) shows that it is essentially the shell motion that governs the mode. It means physically that the stiffness of the springs at the junctions is not strong enough to connect efficiently the shell with the floor, consequently, each substructure vibrates in its own way. Region B can be considered as a transition, in which the frequency increases in a sensitive manner with the increase of the spring stiffness parameter. With $\bar{k} = 10^3$, an observation of the mode shape in Figure 4(b) illustrates that the generated mode is a coupled one involving motion of the shell and the floor. The last region observed is C,

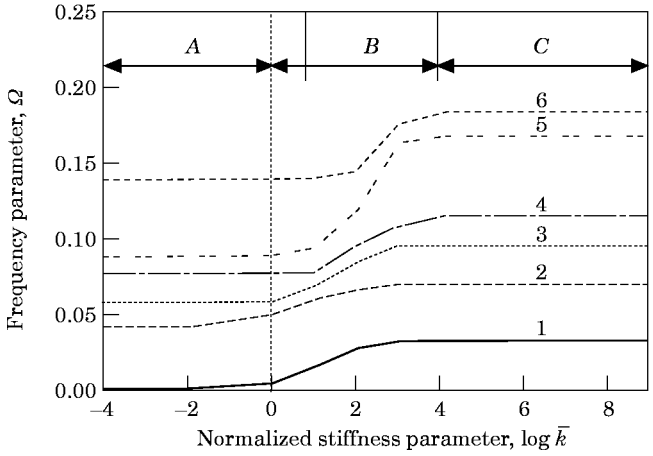

Figure 3. The frequency parameter as functions of the stiffness parameter.

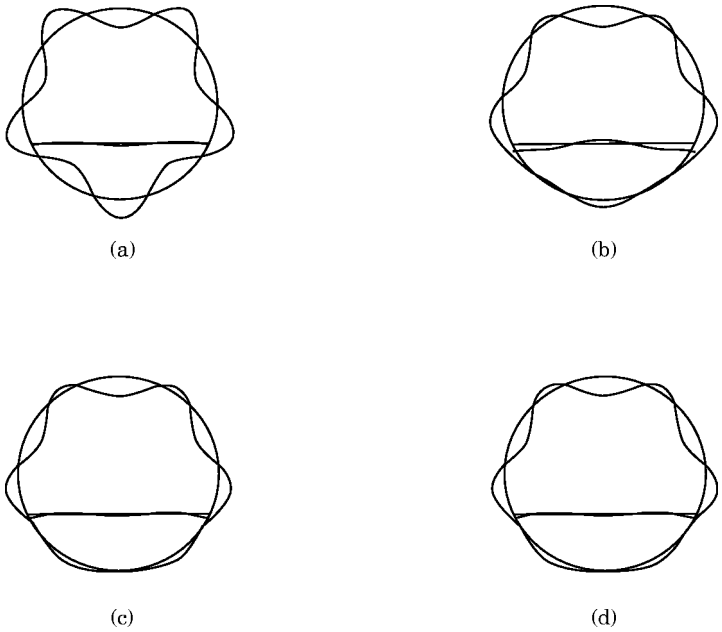

Figure 4. Typical mode shapes in the three regions for the sixth symmetric mode. (a) $\bar{k}=10^{-4}$, $\Omega=0{\cdot}138$; (b) $\bar{k}=10^{3}$, $\Omega=0{\cdot}176$; (c) $\bar{k}=10^{6}$, $\Omega=0{\cdot}184$; (d) $\bar{k}=10^{9}$, $\Omega=0{\cdot}184$.

in which the frequency seems to be stable with the increase of the stiffness. This is understandable, since the stiffness at the junction is already high enough with respect to the stiffness of the system so that a rigid attachment is reached. With two stiffness values in region C ($\bar{k}=10^{6}$ and $\bar{k}=10^{9}$). It is demonstrated in Figure 4(c) and 4(d) that there are no significant changes in mode shapes. In both cases, the continuity between the shell and the floor seems to be assured. When comparing the different curves in Figure 3, one notices a shift of the region C towards higher values of the stiffness parameters when the mode order increases. This can be explained by the fact that the higher order modes have higher stiffnesses so that more stiff springs are needed to realize a rigid attachment. In the calculations, an appropriate value which is high enough for all considered modes can therefore be used to characterize a rigid attachment. The same investigation is done for the *antisymmetric* modes, giving essentially the same behavior of the frequency parameter as function of the stiffness parameter.

For rigid attachment modelling, numerical calculations are carried out to examine the continuity between the shell and the floor with the appropriate stiffness value determined previously. For this purpose, the relative translational motion in the yz cross-section between the shell and the floor (d_y, d_z), which has been already defined in equation (4), is normalized with respect to the maximum displacement of each mode. In the same way, the relative rotation (d_r) between the shell and the floor is normalized with respect to the rotation angle at the junction. All of these values are zero if a rigid attachment is faithfully simulated. The result is shown for the first ten symmetric modes and the first ten antisymmetric modes, in Table 1. It can be seen that all the values reported in the table are really small, indicating that the relative motion becomes negligible with respect to the real motion of the structure. In such a way, one can obtain confidence in the computational accuracy of the present approach to characterize structural coupling.

In order to validate the developed model in a more general way, comparisons between the present analysis and other available results in the literature are made. Moreover, a

TABLE 1

The normalized relative motion between the shell and the floor at the junction: *S*, *symmetric modes*; *A*, *antisymmetric modes*

Mode	$\bar{d}_y$	$\bar{d}_z$	$\bar{d}_r$
1*S*	$1{\cdot}01\times10^{-8}$	$3{\cdot}03\times10^{-8}$	$6{\cdot}64\times10^{-10}$
2*S*	$9{\cdot}44\times10^{-8}$	$5{\cdot}42\times10^{-9}$	$3{\cdot}29\times10^{-10}$
3*S*	$2{\cdot}67\times10^{-8}$	$2{\cdot}12\times10^{-9}$	$7{\cdot}06\times10^{-10}$
4*S*	$5{\cdot}19\times10^{-8}$	$5{\cdot}27\times10^{-10}$	$2{\cdot}04\times10^{-10}$
5*S*	$3{\cdot}48\times10^{-8}$	$3{\cdot}88\times10^{-7}$	$7{\cdot}22\times10^{-10}$
6*S*	$6{\cdot}29\times10^{-7}$	$4{\cdot}95\times10^{-8}$	$3{\cdot}37\times10^{-10}$
7*S*	$8{\cdot}17\times10^{-7}$	$4{\cdot}49\times10^{-7}$	$1{\cdot}40\times10^{-9}$
8*S*	$7{\cdot}81\times10^{-7}$	$2{\cdot}47\times10^{-7}$	$1{\cdot}58\times10^{-9}$
9*S*	$1{\cdot}98\times10^{-6}$	$1{\cdot}27\times10^{-8}$	$2{\cdot}65\times10^{-10}$
10*S*	$1{\cdot}54\times10^{-7}$	$5{\cdot}62\times10^{-8}$	$4{\cdot}37\times10^{-10}$
1*A*	$5{\cdot}21\times10^{-8}$	$6{\cdot}28\times10^{-8}$	$5{\cdot}97\times10^{-11}$
2*A*	$8{\cdot}72\times10^{-8}$	$6{\cdot}70\times10^{-8}$	$2{\cdot}91\times10^{-10}$
3*A*	$1{\cdot}31\times10^{-7}$	$1{\cdot}65\times10^{-7}$	$8{\cdot}71\times10^{-10}$
4*A*	$4{\cdot}19\times10^{-7}$	$1{\cdot}28\times10^{-8}$	$6{\cdot}40\times10^{-10}$
5*A*	$5{\cdot}26\times10^{-7}$	$7{\cdot}41\times10^{-8}$	$1{\cdot}00\times10^{-9}$
6*A*	$2{\cdot}10\times10^{-7}$	$1{\cdot}53\times10^{-8}$	$7{\cdot}08\times10^{-10}$
7*A*	$3{\cdot}79\times10^{-7}$	$2{\cdot}39\times10^{-8}$	$7{\cdot}14\times10^{-10}$
8*A*	$3{\cdot}27\times10^{-7}$	$3{\cdot}37\times10^{-7}$	$2{\cdot}35\times10^{-10}$
9*A*	$2{\cdot}27\times10^{-7}$	$9{\cdot}35\times10^{-7}$	$1{\cdot}32\times10^{-9}$
10*A*	$7{\cdot}22\times10^{-8}$	$1{\cdot}10\times10^{-7}$	$6{\cdot}45\times10^{-10}$

Finite Element Analysis (FEA) using I-DEAS [22] is also performed to provide a base of comparison. The results are summarised in Table 2, in which the frequency parameters for the first eight modes with one half longitudinal wave ($m=1$) are included. In each case, the results of the present analysis are compared to the data taken from reference [7,8] and the FEA simulation. The finite element results are taken as reference to calculate the percentage error (a dash in Table 2 indicates non-available data). As to the finite element simulation, quadrilateral shell elements are used for the shell and the floor. A 46×30 (in the circumferential and longitudinal directions) mesh is used for the shell and a 12×30 (in the transverse and the longitudinal edge directions) mesh for the floor. It can be seen in Table 2 that there is good agreement between our approach, Langley's work and the finite element method for all modes considered. In fact, the three methods give results that agree well within 2·6%. However, one can notice a clear deviation of the results obtained

TABLE 2

A comparison of the frequency parameters

		Peterson		Langley		Present work	
Mode	I-DEAS, Ω	Ω	Error (%)	Ω	Error (%)	Ω	Error (%)
1*S*	0·0326	0·0367	11·17	0·0321	1·55	0·0334	2·39
2*S*	0·0716	0·0693	3·30	0·0713	0·42	0·0715	0·14
3*S*	0·0965	0·0939	2·77	0·0949	1·68	0·0958	0·73
4*S*	0·1180	0·1170	0·85	0·1160	1·72	0·1150	2·60
1*A*	0·0610	0·0625	2·40	—	—	0·0606	0·66
2*A*	0·0785	0·0828	5·20	—	—	0·0805	2·48
3*A*	0·1040	0·1030	0·97	—	—	0·1050	0·95
4*A*	—	0·1330	—	—	—	0·1330	—

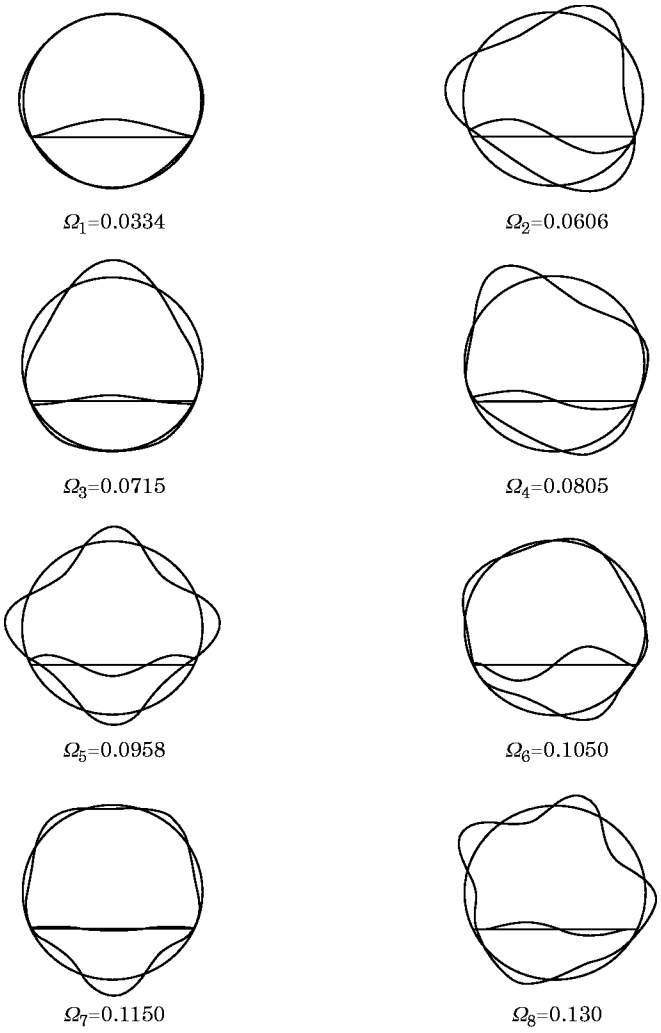

Figure 5. The mode shapes of the partitioned shell.

by Peterson [7], particularly for the fundamental mode. This is due to an error committed in the compatibility equations in his work, which has been equally pointed out and criticized by Langley [8]. The corresponding mode shapes for the same modes are plotted in Figure 5. They are essentially the same as those obtained by Peterson and the finite element method. A more detailed examination of Figure 5 results in a general idea of the kinds of modes that one can encounter for a combined structure, an analysis of which is certainly helpful to the understanding of the coupling phenomena. By examining the mode shapes of the partitioned shell, one can see that the lowest frequency corresponds to a mode which is basically governed by a floor motion. In this case the shell introduces a certain stiffness to the floor, so that the parameter frequency is between a clamped plate and a simply supported one along longitudinal edges. The shell domination appears in the third mode, in which one notices a slight deformation of the floor and a strong motion of the shell. The resulting mode should be qualified as a shell-controlled one. The second mode, however, is a strongly coupled one, in which the two components vibrate at a comparable level. Similar observations have been made in a previous work [18] for a plate-ended shell,

and the physical explanations reported in that paper apply also to the present analysis. Basically, different types of modes for a combined structure depend mainly on the degree of impedance matching between each uncoupled substructure.

This section discusses the effect of distributed springs in a specified direction on the frequencies and mode shapes of the partitioned shell. As shown previously, each mode involves a different kind of coupling. Naturally, the dependence of the modes on the distributed spring should also be different. For illustrating purpose, two modes of different nature are chosen. The procedure is to fix three stiffness parameters at a high value, simulating a rigid attachment in the corresponding directions and allowing a range of variation for the fourth one. This procedure is applied to the fundamental mode and the third mode. During the analysis, it was found that longitudinal springs $\bar{k}_x$ had a negligible effect on these two modes; consequently, no curves are presented here for $\bar{k}_x$. As can be seen from Figure 6 for the fundamental mode, the effect of the vertical structural coupling $\bar{k}_z$ is more obvious than the rotational $\bar{k}_r$ and the horizontal $\bar{k}_y$. The parameter frequency seems insensitive to the variation of the horizontal stiffness. To illustrate the effect of each spring on the mode shapes of the combined system for each direction, in Figure 7 are shown the mode shapes formed by using three points taken from Figure 6 corresponding to 10^{-4}, 10^{1} and 10^{9}, simulating three connections. The evolution of the deformation illustrates the same dependence of the modes shapes on the coupling stiffness as the frequency parameters. More specifically, one notices a neglected influence of the horizontal coupling (Figure 7(a)), a more noticeable effect of the rotational one (Figure 7(c)) and a strong dominance of the vertical (Figure 7(b)) one. The same procedure is followed to analyze the third mode, which is a coupled one. In Figures 8 and 9 it is shown that it is the horizontal stiffness that is the most important one among the three others. The results seem to indicate that the direction in which there is the strongest impedance mismatch calls for a dominant effect of the stiffness in that direction.

The following results discuss the effect of the in-plane motion of the floor on the frequencies of the combined system. In the developed formulation, both flexural and in-plane motion of the floor has been considered. However, it is logical to suppose that the in-plane stiffness of the floor should be much greater than that of the flexion, which may provide further simplifications for the calculations. In order to investigate this case, both symmetric and antisymmetric modes are analyzed. In Figure 10(a) the frequency

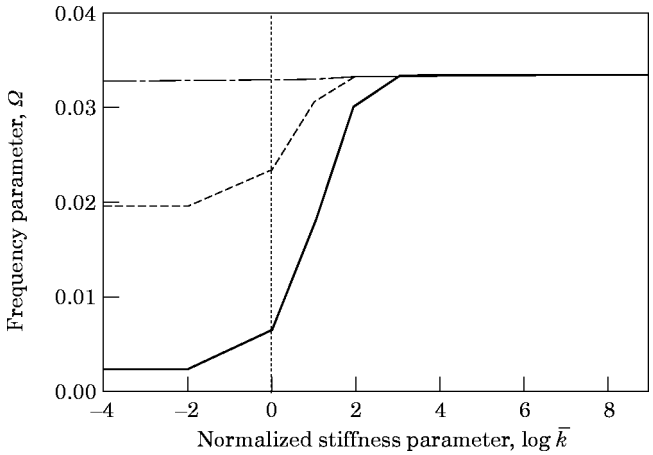

Figure 6. The frequency variation of the fundamental mode as function of the stiffness parameter. ———, $\bar{k}_z$; — — —, $\bar{k}_r$; — · — · —, $\bar{k}_y$.

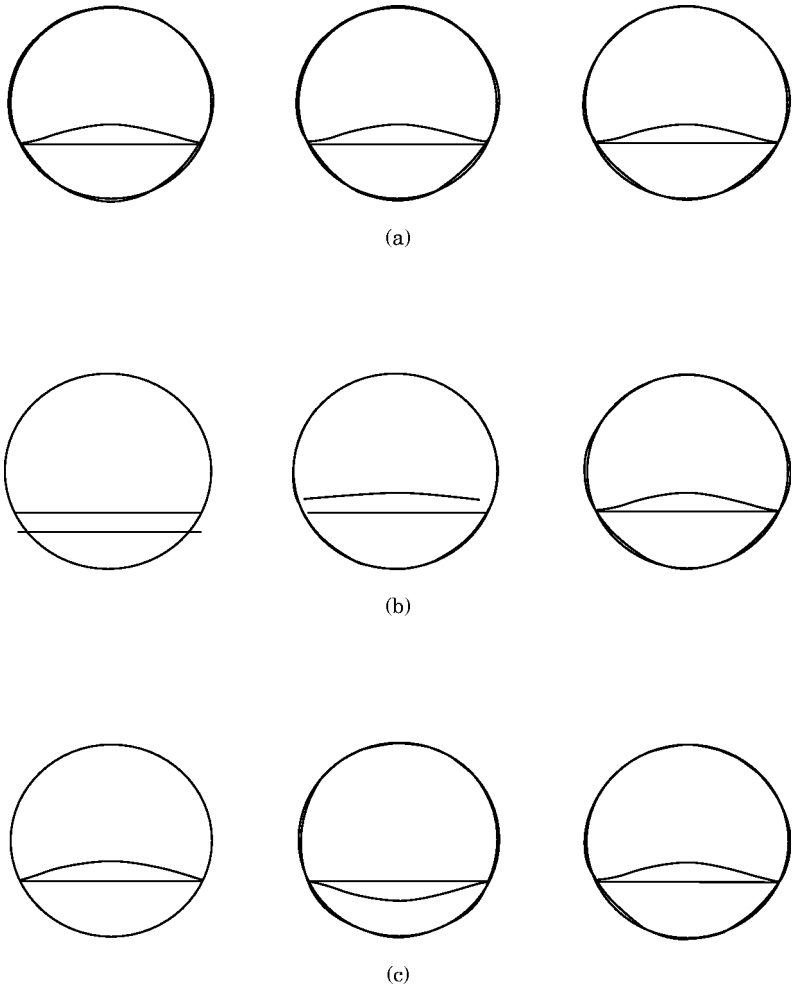

Figure 7. The effect of the spring parameters on the fundamental mode shape. From left to right: (a) $\bar{k}_y = 10^{-4}$, $\bar{k}_y = 10^{1}$, $\bar{k}_y = 10^{9}$; (b) $\bar{k}_z = 10^{-4}$, $\bar{k}_z = 10^{1}$, $\bar{k}_z = 10^{9}$; (c) $\bar{k}_r = 10^{-4}$, $\bar{k}_r = 10^{1}$, $\bar{k}_r = 10^{9}$.

parameters for the first ten symmetric modes with and without the in-plane motion of the floor are compared (in Figure 10(a), *TB* means "only transversal bending" and *IPM* means "including in-plane motion"). It can be seen that neglecting the in-plane motion of the floor introduces no visible change in the frequency for all the considered modes. Hence, the in-plane parameters of the floor can be neglected in the calculations of symmetric modes as a good approximation. The same investigations are carried out for the antisymmetric modes, and results are presented in Figure 10(b). It is clear that the in-plane motion of the floor has, in this case, significant effects on the natural frequency. In fact, the inclusion of the in-plane motion brings down considerably the natural frequency of the combined structure. This is understandable, since neglecting the in-plane motion of the floor implies fixing the floor in the horizontal direction, so that the floor acts as a rigid support in the horizontal direction of the shell. As a result, the natural frequency of the structure is increased. It should be stressed that, physically, the so-called in-plane motion of the floor along the horizontal direction has two meanings: first, it implies a rigid body motion for all points lying in the same horizontal line; second, it includes the membrane

deformation (extension–compression). For the antisymmetric modes, the rigid body motion may be important. This analysis is confirmed in Figure 10(c) in which only the rigid body in-plane motion (*RIPM*) of the floor is kept while eliminating the membrane effect. It can be seen that considering only the rigid part of the in-plane motion of the floor gives satisfactory results with respect to the full coupling analysis. From these results we arrive at the following conclusions: for the lower order modes, the in-plane effect can be neglected for the symmetric modes. However, the in-plane effect is important for antisymmetric modes; this even for the low order modes. In this case, the main effect comes from the rigid body motion of the floor, behaving itself as a local mass. The membrane motion, in its turn, is a negligible factor. From the point of view of numerical calculations, this observation suggests that the truncation of the series for the in-plane displacement should include at least the rigid body motion of the floor in the horizontal direction. By doing this, a limited number of terms in the u_f and v_f decomposition series should be sufficient to obtain good results for a low frequency range.

The following calculations study the structural response under a point excitation. The procedure consists of comparing, first, the vibration levels of the shell with and without the floor; second, the floor behavior is compared to the shell when the system is structurally coupled. These simulations show the effects of the floor on the structural response. The dynamic load is an unit harmonic radial force applied at the external surface of the shell at the point ($x_{si} = L_s/5$, $\theta_{si} = 20^\circ$). The average quadratic velocity is calculated by only considering the radial component for the shell and the transverse component for the floor in certain cases. The material properties and the geometry are the same as the ones used previously, while the maximum terms used in equations (1) and (2) are truncated to $m^* = 10$, $n_s^* = n_w^* = 20$, $n_u^* = n_v^* = 5$, for a good convergence. The structural damping factor of each subsystem has been set to be 0·01. The average quadratic velocity is expressed in dB, referenced to a quadratic velocity $5 \times 10^{-9} \mathrm{m}^2/\mathrm{s}^2$. The vibration levels of the shell with and without the floor partition are compared in Figure 11. It can be seen that, compared to the single shell, the inclusion of the floor into the model does not basically change the general trend of the overall vibration level of the shell. However, a detailed examination of the two curves shows that the floor has a visible effect on the shell response. More specifically, due to the coupling introduced by the floor, resonance peaks are shifted. Moreover, additional resonance dominated by the floor motion can be clearly

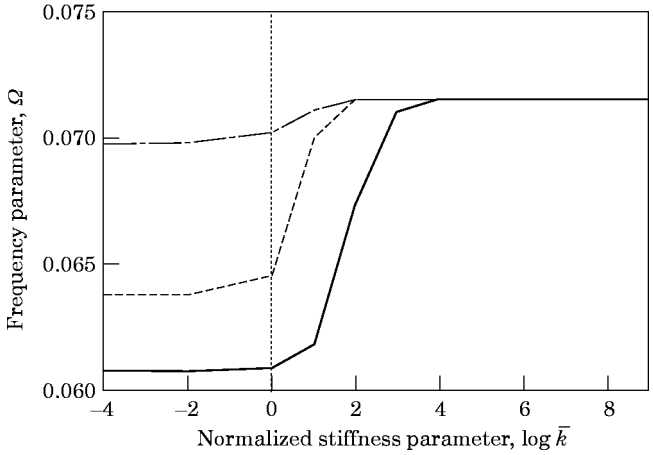

Figure 8. The frequency variation of the third mode as function of the stiffness parameter. ———, $\bar{k}_y$; – – – –, $\bar{k}_z$; — · — · —, $\bar{k}_r$.

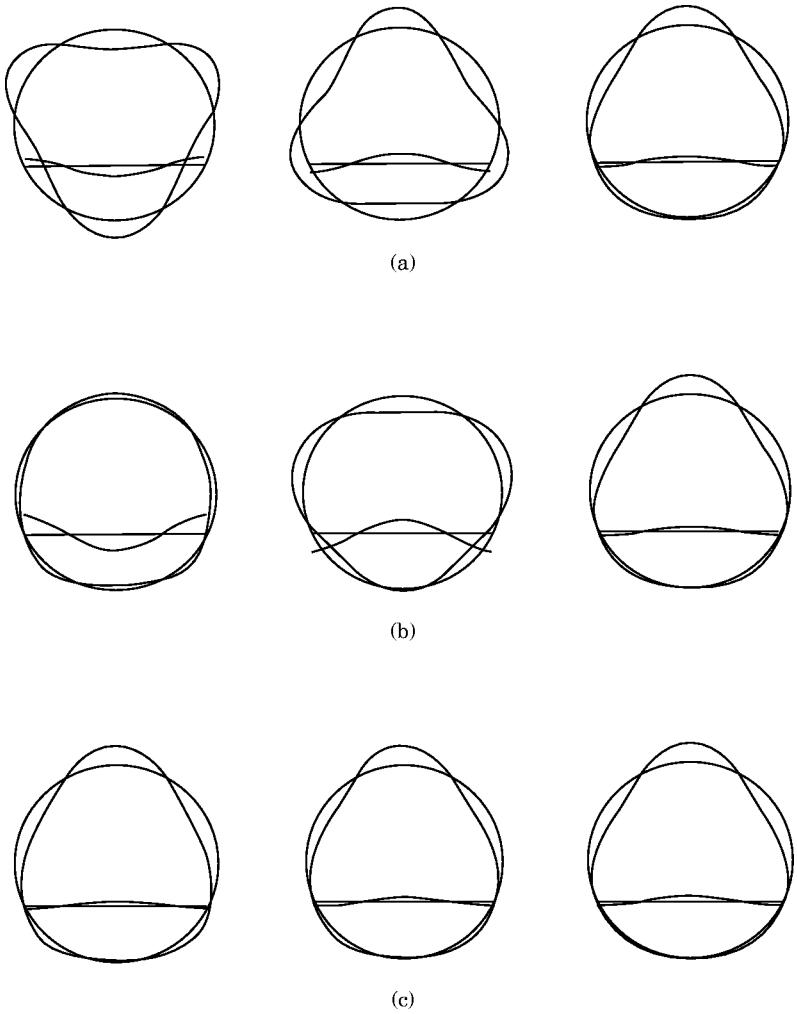

Figure 9. The effect of the spring parameters on the third mode shape. From the left to right: (a) $\bar{k}_y = 10^{-4}$, $\bar{k}_y = 10^{1}$, $\bar{k}_y = 10^{9}$; (b) $\bar{k}_z = 10^{-4}$, $\bar{k}_z = 10^{1}$, $\bar{k}_z = 10^{9}$; (c) $\bar{k}_r = 10^{-4}$, $\bar{k}_r = 10^{1}$, $\bar{k}_r = 10^{9}$.

identified. The local response can be considerably disturbed by the floor. The vibrational response of the combined structure, in which the vibration level of the shell is compared to that of the floor, is illustrated in Figure 12. It can be seen that at the low and the middle frequencies (< 1000 Hz), the vibration levels for both substructures are of the same order of magnitude, indicating that the structural coupling between substructures is strong. However, at high frequencies, the shell which is directly excited is more active than the floor. Combining the two figures, the following observations can be made. First, from the point of view of dynamic analysis, if one is only interested in the shell vibration of a shell–floor combination, such as the one modelled in this paper, the single-shell model seems to be sufficient roughly to estimate the overall vibration level unless better precision is needed. This justifies the common practice of using a single shell as a primary model to predict dynamic properties of an airplane fuselage reported in numerous papers. However, from the point of view of noise prediction in the cabin, the fact that the floor can vibrate as strongly as the shell at low and middle frequency ranges indicates that the

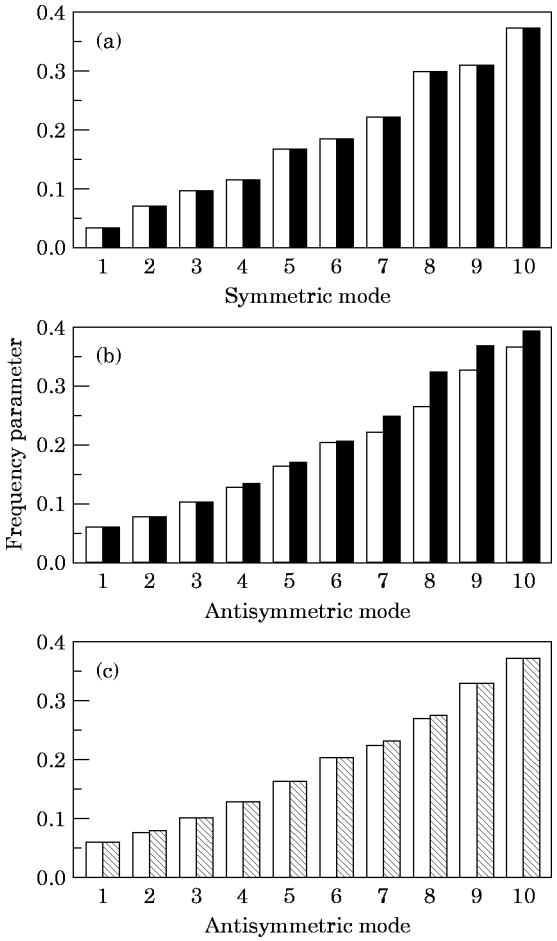

Figure 10. The effect of the in-plane motion of the floor on structural modes. (a) Symmetric modes; (b) and (c) antisymmetric modes. ■, *TB* only transversal bending; □, *TB* and *IPM* transversal bending and in-plane motion; ▨, *TB* and *RIPM* transversal bending and rigid in-plane motion.

floor could be an important component to be modelled at the same time as the fuselage, since the floor may also be a strong sound radiator.

6. CONCLUSIONS

The concept of artificial spring systems is applied to the analysis of a complex structure comprising a cylindrical shell and an internal longitudinal floor partition. The formulation is based on the variational principle. With the use of an artificial spring system, the characterization of the coupling conditions between the shell and the floor becomes systematic, providing various possibilities for analyzing the different connections. Efforts have been made to assess the feasibility and the efficiency of the method, as well as to reveal some physical phenomena of the system. The main conclusions of the investigations are summarized as follows.

(1) The comparison with other available approaches shows that, with the proper assignation of the spring stiffness, the formulation allows an accurate simulation of the rigid attachment. In addition to a wide range of variation of modelling of the coupling,

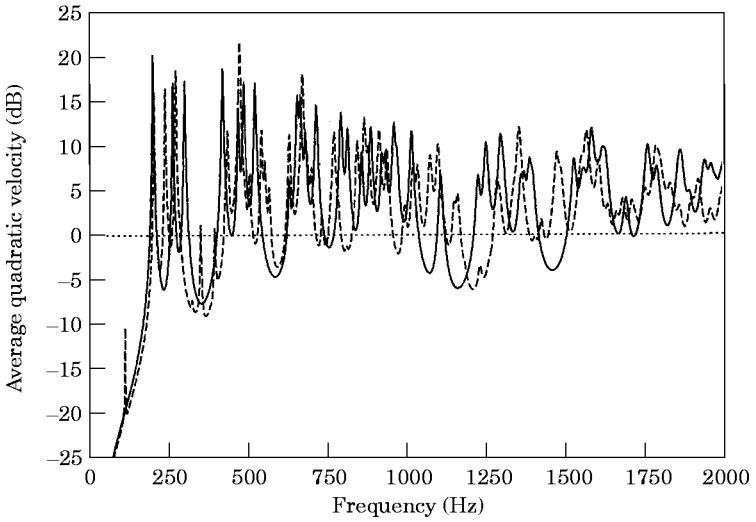

Figure 11. The average quadratic velocity of the shell. ———, Single shell; – – – –, shell with a floor partition.

the rigid attachments can be simulated reasonably well with high values of spring stiffnesses.

(2) Different stiffness values used at the floor–shell connection generally affect the natural frequency and the mode shapes of the combined structure. Although each mode involves different coupling mechanisms, it is observed that when the spring stiffness increases, the resulting mode undergoes generally three regions: for a very weak stiffness, the system behaves mainly as two separate structures; for the intermediate region, coupling between the substructures becomes more obvious, with a rapid increase of the natural frequencies with the stiffness; and the third region corresponds to a rigid attachment, characterized by a relatively stable value of the natural frequency, in which a further increase of the spring stiffness does not noticeably change the natural frequency.

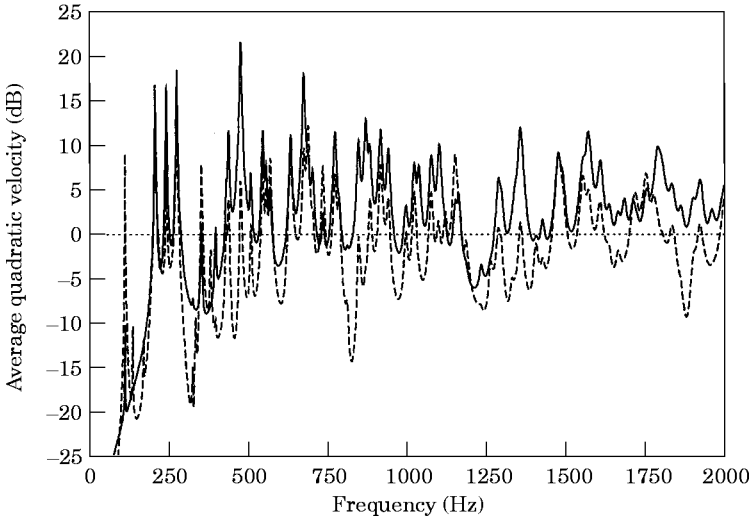

Figure 12. The average quadratic velocity of the combined structure, ———, Shell; – – – –, floor.

(3) As far as the effect of the spring stiffness in different directions is concerned, the mode is most sensitive to changes of the spring stiffnesses in the direction in which the impedance mismatch is most strong between the shell and the floor.

(4) The in-plane motion of the floor seems to be negligible for lower order modes, except for antisymmetric ones. In the later case, the rigid body motion along the horizontal direction should be considered in the calculation.

(5) In the low and middle frequency range (where the structure exhibited strong modal behavior), the floor is strongly coupled to the shell with a comparable vibration level. With increase of frequency, the coupling becomes weaker.

Finally, one of the appealing featrues of the method lies in its capability to handle vibro-acoustic analysis when an acoustic medium is included in the model. The topic is particularly important for soundproofing in an airplane cabin. The next step of our research will focus on this issue.

ACKNOWLEDGEMENT

The authors wish to thank the National Science and Engineering Research Council of Canada for supporting this work.

REFERENCES

1. L. R. Koval 1978 *Journal of Sound and Vibration* **59**, 23–33. Effects of cavity resonances on sound transmission into a thin cylindrical shell.
2. L. D. Pope, D. C. Rennison and E. G. Wilby 1980 *NASA CR* 159363. Analytical prediction of the interior noise for cylindrical models of aircraft fuselages for prescribed exterior noise fields—phase I: development and validation of preliminary analytical models.
3. F. J. Balena, R. A. Prydz and J. D. Revell 1983 *Journal of Aircraft* **20**, 434–439. Single and double wall cylinder noise reduction.
4. S. Narayanan and R. L. Shanbhag 1984 *Journal of Sound and Vibration* **92**, 541–558. Sound transmission through layered cylindrical shells with applied damping treatment.
5. B. Laulagnet and J. L. Guyader 1989 *Journal of Sound and Vibration* **131**, 397–415. Modal analysis of a shell's acoustic radiation in light and heavy fluids.
6. D. R. Thomas, P. A. Nelson and S. J. Elliott 1993 *Journal of Sound and Vibration* **167**, 91–111. Active control of the transmission of sound through a thin cylindrical shell, part I: the minimization of vibrational energy.
7. M. R. Peterson and D. E. Boyd 1978 *Journal of Sound and Vibraiton* **60**, 45–62. Free vibrations of circular cylinders with longitudinal, interior partitions.
8. R. S. Langley 1992 *Journal of Sound and Vibration* **156**, 521–540. A dynamic stiffness technique for the vibration analysis of stiffened shell structures.
9. T. Irie, G. Yamada and Y. Kobayashi 1984 *Journal of Sound and Vibration* **96**, 133–142. Free vibration of non-circular cylindrical shells with longitudinal interior partitions.
10. J. F. Unruh and S. A. Dobosz 1988 *Journal of Vibration, Acoustics, Stress and Reliability in Design* **110**, 226–233. Fuselage structural-acoustic modelling for structure-borne interior noise transmission.
11. D. T. Huang and W. Soedel 1993 *Journal of Sound and Vibration* **163**, 403–427. Natural frequencies and modes of a circular plate welded to a circular cylindrical shell at arbitrary axial positions.
12. D. J. Gorman 1989 *Journal of Applied Mechanics* **56**, 839–399. A comprehensive study of the free vibration of rectangular plates resting on symmetrically-distributed uniform elastic supports.
13. G. B. Warburton and S. L. Edney 1984 *Journal of Sound and Vibration* **95**, 537–552. Vibrations of rectangular plates with elastically restrained edges.
14. T. Mizusawa 1979 *Journal of Sound and Vibration* **62**, 301–308. Vibration of skew plate by using B-spline functions.
15. T. Irie, G. Yamada and T. Tanaka 1984 *Journal of Sound and Vibration* **95**, 249–259. Free vibration of a circular cylindrical double-shell system interconnected by several springs.

16. J. YUAN and S. M. DICKINSON 1992 *Journal of Sound and Vibration* **153**, 203–216. On the use of artificial springs in the study of the free vibrations of systems comprised of straight and curved beams.
17. J. YUAN and S. M. DICKINSON 1992 *Journal of Sound and Vibration* **159**, 39–55. The flexural vibration of rectangular plate systems approached by using artificial springs in the Rayleigh-Ritz method.
18. L. CHENG and J. NICOLAS 1992 *Journal of Sound and Vibration* **155**, 231–247. Free vibration analysis of a cylindrical shell-circular system with general coupling and various boundary conditions.
19. L. CHENG 1994 *Journal of Sound and Vibration* **174**, 641–654. Fluid–structural coupling of a plate-ended cylindrical shell: vibration and internal sound field.
20. A. W. LEISSA 1973 *Journal of Sound and Vibration* **31**, 257–293. The free vibration of rectangular plates.
21. L. MEIROVITCH 1969 *Analytical Methods in Vibrations*. New York: Macmillan.
22. I-DEAS, *SDRC*, 2000 Eastman Drive Milford, Ohio 45150, U.S.A.

APPENDIX A: TERMS IN EQUATIONS (7)

$$S^x_{mn_s n'_s \alpha} = k_x L_s a_{mn_s} a_{mn'_s} \cos\left(n_s\phi - \alpha\frac{\pi}{2}\right)\cos\left(n'_s\phi - \frac{\alpha\pi}{2}\right),$$

$$S^y_{mn_s n'_s \alpha} = k_y L_s \left[\sin\phi\cos\left(n_s - \alpha\frac{\pi}{2}\right) + b_{mn_s}\cos\phi\sin\left(n_s - \alpha\frac{\pi}{2}\right)\right]\left[\sin\phi\cos\left(n'_s - \alpha\frac{\pi}{2}\right)\right.$$

$$\left. + b_{mn'_s}\cos\phi\sin\left(n'_s - \alpha\frac{\pi}{2}\right)\right],$$

$$S^z_{mn_s n'_s \alpha} = k_z L_s \left[b_{mn_s}\sin\phi\sin\left(n_s\phi - \alpha\frac{\pi}{2}\right) - \cos\phi\cos\left(n_s\phi - \alpha\frac{\pi}{2}\right)\right]\left[b_{mn'_s}\sin\phi\sin\right.$$

$$\left.\times\left(n'_s\phi - \alpha\frac{\pi}{2}\right) - \cos\phi\cos\left(n'_s - \alpha\frac{\pi}{2}\right)\right],$$

$$S^r_{mn_s n'_s \alpha} = \frac{k_r L_s}{a^2}\left[(b_{mn_s} + n_s)(b_{mn'_s} + n'_s)\sin\left(n_s\phi - \alpha\frac{\pi}{2}\right)\sin\left(n'_s\phi - \alpha\frac{\pi}{2}\right)\right],$$

$$k^u_{mn_f n'_f \alpha} = R^2_{n_f n'_f \alpha} + \frac{K_f\pi^2}{2L_s}\left[m^2\beta_{n_f n'_f \alpha} + \tfrac{1}{2}\left(\frac{L_s}{b}\right)^2 n_f n'_f(1-\nu)\gamma_{n_f n'_f \alpha}\right],$$

$$k^v_{mn_f n'_f \alpha} = R^3_{n_f n'_f \alpha} + \frac{K_f\pi^2}{2L_s}\left[\frac{n_f n'_f}{b^2}\beta_{n_f n'_f \alpha} + \frac{m^2}{2L_s}(1-\nu)\gamma_{n_f n'_f \alpha}\right],$$

$$k^w_{mn_f n'_f \alpha} = R^4_{n_f n'_f \alpha} + \frac{D_f\pi^4}{2}\left[\frac{m^4}{L_s^3} + \frac{m^2}{b^2 L_s}(n_f + n'_f)^2\nu + \frac{L_s}{b^4}n_f^2 n_f'^2\right]\beta_{n_f n'_f \alpha} + \frac{2m^2}{b^2 L_s}(1-\nu)n_f n'_f\gamma_{n_f n'_f \alpha},$$

$$\beta_{n_f n'_f \alpha} = \int_{-b/2}^{b/2} \cos\left(\frac{n_f \pi y}{b} - \alpha\frac{\pi}{2}\right)\cos\left(\frac{n'_f \pi y}{b} - \alpha\frac{\pi}{2}\right)\mathrm{d}y,$$

$$\gamma_{n_f n'_f \alpha} = \int_{-b/2}^{b/2} \sin\left(\frac{n_f \pi y}{b} - \alpha\frac{\pi}{2}\right)\sin\left(\frac{n'_f \pi y}{b} - \alpha\frac{\pi}{2}\right)\mathrm{d}y,$$

$$M_{mn_s} = \frac{\rho L_s \pi h_s a}{\epsilon_{n_s}}(1 + a^2_{mn_s} + b^2_{mn_s}).$$

$$k_f = Eh_f/(1-v^2)$$

APPENDIX B: NOMENCLAUTRE

a	shell radius
b	floor width
$\bar{d}_y, \bar{d}_z, \bar{d}_r$	normalized relative motion in the horizontal, the vertical and the rotational attachment respectively
D_f	$= Eh_f^3/[12(1-v^2)]$
E	Young modulus
F_u^i	longitudinal component of the ith driving force
F_v^i	tangential component of the ith driving force
F_w^i	radial component of the ith driving force
h_s	shell wall thickness
h_f	floor thickness
$\bar{k}(\bar{k}_x, \bar{k}_y, \bar{k}_z, \bar{k}_r)$	normalized spring stiffness parameter
k_r	rotational spring stiffness
k_x	longitudinal spring stiffness
k_y	horizontal spring stiffness
k_z	vertical spring stiffness
K_f	$= Eh_f/(1-v^2)$, membrane stiffness
L_s	shell length
m	longitudinal half-wavenumber
m^*	highest value in the longitudinal series
n_s	circumferential mode number
n_s^*	the highest circumferential term in the series
n_f	terms in the floor series
n_u^*, n_v^*, n_w^*	the highest value of n_f taken for u_f, v_f and w_f, respectively
u_f, v_f, w_f	floor displacements, as illustrated in Figure 2(a)
u_s, v_s, w_s	axial, tangential and radial displacement of the shell
u, θ	cylindrical co-ordinates
ρ	structural material density
v	Poisson ratio
ω	angular frequency
Ω	$a\omega[\rho(1-\omega^2)/E]^{1/2}$ frequency parameter
ϕ	floor angle
α	symmetric or antisymmetric mode index
ϵ_{n_s}	1, if $n_s = 0$; 2, if $n_s > 0$

Subscripts

f	floor
s	shell